

Synthesis and Characterization of Tris-chelate Complexes for Understanding *f*-Orbital Bonding in Later Actinides

Shane S. Galley,[†] Scott A. Pattenaude,[‡] Carlo Alberto Gaggioli,[§] Yusen Qiao,^{||} Joseph M. Sperling,[†] Matthias Zeller,[‡] Srimanta Pakhira,^{⊥,‡} Jose L. Mendoza-Cortes,^{⊥,‡} Eric J. Schelter,^{||} Thomas E. Albrecht-Schmitt,[†] Laura Gagliardi,[§] and Suzanne C. Bart^{*,‡}

[†]Department of Chemistry and Biochemistry, Florida State University, Tallahassee, Florida 32306, United States

[‡]H.C. Brown Laboratory, Department of Chemistry, Purdue University, West Lafayette, Indiana 47907, United States

[§]Department of Chemistry, Supercomputing Institute, and Chemical Theory Center, University of Minnesota, Minneapolis, Minnesota 55455, United States

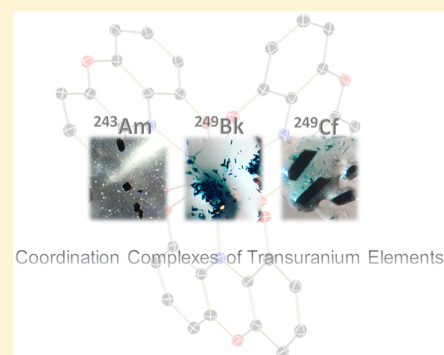
^{||}P. Roy and Diana T. Vagelos Laboratories, Department of Chemistry, University of Pennsylvania, Philadelphia, Pennsylvania 19104, United States

[⊥]Department of Physics, Scientific Computing, Material Sciences and Engineering, High-Performance Material Institute & Condensed Matter Theory - High Magnetic Field National Laboratory, Florida State University, Tallahassee, Florida 32310, United States

[#]Department of Chemical & Biomedical Engineering, Florida A&M University – Florida State University, Joint College of Engineering, Tallahassee, Florida 32310, United States

Supporting Information

ABSTRACT: An isostructural family of *f*-element compounds (Ce, Nd, Sm, Gd; Am, Bk, Cf) of the redox-active dioxophenoxazine ligand (DOPO^q; DOPO = 2,4,6,8-tetra-*tert*-butyl-1-oxo-1*H*-phenoxazin-9-olate) was prepared. This family, of the form M(DOPO^q)₃, represents the first nonaqueous isostructural series, including the later actinides berkelium and californium. The lanthanide derivatives were fully characterized using ¹H NMR spectroscopy and SQUID magnetometry, while all species were structurally characterized by X-ray crystallography and electronic absorption spectroscopy. In order to probe the electronic structure of this new family, CASSCF calculations were performed and revealed these systems to be largely ionic in contrast to previous studies, where berkelium and californium typically have a small degree of covalent character. To validate the zeroth order regular approximation (ZORA) method, the same CASSCF analysis using experimental structures versus UDFT-ZORA optimized structures does not exhibit sizable changes in bonding patterns. This shows that UDFT-ZORA combined with CASSCF could be a useful first approximation to predict and investigate the structure and electronic properties of actinides and lanthanides that are difficult to synthesize or characterize.



INTRODUCTION

Recycling of used nuclear fuels represents significant contributions to the cost and waste generation of nuclear fuel cycles.^{1,2} The application of ligands designed to have a high specificity for separating targeted isotopes from the complex mixture of elements in used fuel has been successful, but lack of understanding about the basic coordination chemistry of certain heavy elements, especially those beyond uranium, has hindered progress.^{2–5} As established by studies in the *d*-block, ionic radius, oxidation state, electronegativity, valence electron configuration, and other factors determine the coordination environment of a metal. Thus, to effectively design ligands for binding transuranium elements, these characteristics must be understood on a fundamental level.

Trends for these properties have been well established for *d*-block elements, and many studies have repeatedly highlighted contrasting chemistry between early and late transition metals.^{6,7} The relatively fewer studies on actinides suggest that elements early in the series take on covalent character, due to mixing of the 6*p*, 6*d*, and 5*f* orbitals for bonding to organic ligands.^{3,4,8,9} As the actinide series is traversed, the later elements begin to behave more like lanthanides, where the 3+ oxidation state and ionic bonding character dominate. Elements past plutonium are known to have similar chemical properties with lanthanides, causing separation of so-called minor actinides (Np, Pu, Am, Cm) and lanthanides present in

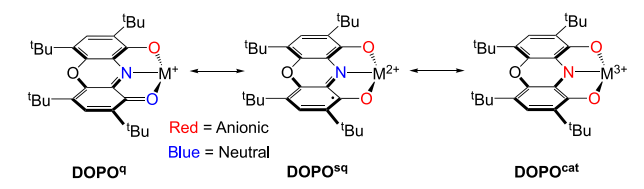
Received: September 26, 2018

Published: February 4, 2019

used nuclear fuel to be challenging. While actinides are typically associated with higher degrees of covalency in their metal–ligand bonds as compared to the lanthanides, leveraging this property for separations of trivalent ions is challenging because the degree of covalency is known to decrease with the lowering of the oxidation state for actinides.¹⁰

Recent work in the actinide series featuring tris(dipicolinate)[2,6-pyridinedicarboxylic acid] (H_2dpa) complexes, $An(Hdpa)_3$ ($An = Am, Cm, Cf, Bk$), has demonstrated that while the above trend is generally true for transuranium elements, the availability of the +2 oxidation state for californium causes a deviation that overrides the minor contraction of the $5f$ orbitals that is typically observed.^{11,12} Additionally, more recent studies have shown that as the actinide series is traversed, the $5f$ orbitals lower in energy, approaching the energy of the $2p$ orbitals of common ligand groups. We hypothesized that using later actinides with redox-active ligands, those that accept electron density into their empty π^* orbitals, may facilitate some degree of covalent bonding in actinide–ligand bonds, which are typically known to be ionic. Such a class of ligands have been shown to produce highly covalent transition-metal compounds.¹³ The dioxophenoxazine (DOPO) ligand (DOPO = 2,4,6,8-tetra-*tert*-butyl-1-oxo-1*H*-phenoxazin-9-olate) is an appropriate choice, given its widespread use on d -^{14,15} and f -block^{16–18} metals. This ligand's planar coordination mode, its ability to form robust metal–oxygen bonds, and its analogy to dipicolinate make it attractive for this study. The redox flexibility of this ligand is key to its function, as it can take on three different oxidation states: -1 , as the quinone resonance form, $DOPO^q$; -2 as the open shell semiquinone, $DOPO^{sq}$, where a radical resides in the π^* of the ligand; and -3 as the closed shell catechol form, $DOPO^{cat}$, where two electrons are paired in the π^* orbital (Scheme 1).

Scheme 1. Resonance Structures for DOPO Ligand



Subsequent to the synthesis of tris(dipicolinate) derivatives, we prepared a new family of trivalent lanthanide (Ce, Nd, Sm, Gd) and actinide (Am, Bk, Cf) coordination compounds featuring the dioxophenoxazine (DOPO) ligand. We postulated that the large ionic radii of the f -block metals would permit formation of tris(DOPO) complexes, and that the redox flexibility of the ligands would allow for the isolation of an isostructural set across the lanthanide and actinide series. Tris-ligand complexes of similar ONO-chelating ligands (ONO = 3,5-di-*tert*-butyl-1,2-quinone-1-(2-oxy-3,5-di-*tert*-butylphenyl)imine) have been characterized for strontium and samarium, while bis-ligand complexes for both DOPO and ONO are reported for many other metals.^{14,15} These homoleptic tris(ligand) compounds, of the form $M(DOPO^q)_3$, have been fully characterized using structural, spectroscopic, and magnetic techniques as well as electronic structure theory calculations. Our findings highlight trends in bonding and covalency between the different regions of the f -block.

EXPERIMENTAL SECTION

General Considerations. All manipulations were performed using standard Schlenk techniques or in an MBraun inert atmosphere drybox with an atmosphere of purified nitrogen (lanthanides) or ultrahigh purity argon (transuranics). Gadolinium chloride (99.9%), samarium chloride (99.9%), neodymium chloride (99.9%), and cerium chloride (99.9%) were purchased from Strem Chemicals. Pentane and toluene were dried and deoxygenated using literature procedures with a Seca solvent purification system.¹⁹ Anhydrous pyridine was purchased from Sigma-Aldrich and was used without further purification. Benzene- d_6 was purchased from Cambridge Isotope Laboratories and was degassed by three freeze–pump–thaw cycles and dried over molecular sieves and sodium. 2,4,6,8-Tetra-*tert*-butyl-9-hydroxy-1*H*-phenoxazin-1-one ($HDOPO^q$) was prepared according to literature procedures.²⁰

Caution! ²⁴³Am ($t_{1/2} = 7380$ years), ²⁴⁹Bk ($t_{1/2} = 320$ days), and ²⁴⁹Cf ($t_{1/2} = 351$ years) represent serious health risks due to their α emission and the radiotoxicity associated with their α , β , and γ emitting daughters. All studies with these actinides were conducted in a laboratory dedicated to studies on transuranic elements. This laboratory is located in a nuclear science facility at Florida State University and is equipped with HEPA-filtered hoods and gloveboxes. A series of instruments continually monitor the radiation levels in the laboratory. All free-flowing actinide solids are handled in gloveboxes, and products are only examined when coated with immersion or krytox oil. Significant limitations exist to accurately determine the yields of these actinide compounds because drying, isolating, and weighing a solid are required, which creates an inhalation hazard and manipulation difficulties given the small quantities of products from these reactions.

NMR Spectroscopy. ¹H NMR spectra were recorded on a Varian Inova 300 spectrometer at 299.992 MHz. All chemical shifts are reported relative to the peak for SiMe₄, using ¹H (residual) chemical shifts of the solvent as a secondary standard. The spectra for paramagnetic molecules were obtained using an acquisition time of 0.5 s; thus, the peak widths reported have an error of ± 2 Hz. For paramagnetic molecules, the ¹H NMR data are reported with the chemical shift, followed by the peak width at half height in hertz, the integration value, and, where possible, the peak assignment.

Electronic Absorption Spectroscopy. Electronic absorption measurements were recorded at 294 K with a Craic Technologies microspectrophotometer. Single crystals of each compound were placed on a quartz slide in immersion oil, and the data were collected from 300 to 1100 nm.

X-ray Crystallography. A single crystal of $Ce(DOPO^q)_3$ for X-ray diffraction was coated with poly(isobutene) oil in a glovebox and transferred to the goniometer head of a Bruker AXS D8 Quest CMOS diffraction equipped with a complementary metal-oxide-semiconductor (CMOS) detector and an I- μ -S Mo $K\alpha$ microsource X-ray tube ($\lambda = 0.71073$ Å) operated at 50 kV and 1 mA with laterally graded multilayer (Goebel) mirror X-ray optics. Data were collected, reflections were indexed and processed, and the files scaled and corrected for absorption using SADABS.²¹ The space group was assigned, and the structure was solved by direct methods using XPREP within the SHELXTL suite of programs^{22,23} and refined by full matrix least-squares against F^2 with all reflections using Shelxl2014²⁴ using the graphical interface Shelxle.²⁵ A solvate toluene molecule is disordered. Its two moieties were restrained to have similar geometries as another nondisordered toluene molecule, and the atoms of the disordered moieties were subjected to a rigid bond restraint (RIGU in Shelxl). Subject to these conditions the occupancy ratio refined to 0.624(6) to 0.376(6).

A single crystal of $Nd(DOPO^q)_3$ for X-ray diffraction was coated with poly(isobutene) oil in a glovebox and quickly transferred to the goniometer head of a Rigaku Rapid II image plate diffractometer equipped with a MicroMax002+ high intensity copper X-ray source with confocal optics. Preliminary examination and data collection were performed with Cu $K\alpha$ radiation ($\lambda = 1.54184$ Å). Data were collected using the dtrek option of CrystalClear.²⁶ The data set was

processed using HKL3000, and data were corrected for absorption and scaled using Scalepack.²⁷ The space group was assigned, and the structure was solved by direct methods using XPREP within the SHELXTL suite of programs^{22,23} and refined by full matrix least-squares against F^2 with all reflections using Shelxl2014²⁴ using the graphical interface Shelxle.²⁵

Single crystals of $\text{Sm}(\text{DOPO}^{\text{q}})_3$ and $\text{Gd}(\text{DOPO}^{\text{q}})_3$ for X-ray diffraction were coated with poly(isobutene) oil in a glovebox and quickly transferred to the goniometer head of a Nonius KappaCCD image plate diffractometer equipped with a graphite crystal, incident beam monochromator. Preliminary examination and data collection were performed with Mo $K\alpha$ radiation ($\lambda = 0.71073 \text{ \AA}$). Data were collected using the Nonius Collect software.²⁸ The data set was processed using HKL3000, and data were corrected for absorption and scaled using Scalepack.²⁷ The space group was assigned, and the structure was solved by direct methods using XPREP within the SHELXTL suite of programs^{22,23} and refined by full matrix least-squares against F^2 with all reflections using Shelxl2014²⁴ and the graphical interface Shelxle.²⁵ Two of four solvate pyridine rings were refined as disordered over two slightly rotated orientations. For $\text{Gd}(\text{DOPO}^{\text{q}})_3$, the geometries of all four pyridine rings were restrained to be similar, and the U^{ij} components of the Atomic Displacement Parameters (ADP) of disordered atoms were restrained to be similar for atoms closer to each other than 1.7 Å. Subject to these conditions the occupancy ratio for the rings involving N6 refined to 0.338(10); the ones involving N7 refined to 0.428(8). No restraints were used for $\text{Sm}(\text{DOPO}^{\text{q}})_3$.

Single crystals of $\text{Am}(\text{DOPO}^{\text{q}})_3$, $\text{Bk}(\text{DOPO}^{\text{q}})_3$, and $\text{Cf}(\text{DOPO}^{\text{q}})_3$ were mounted on a Mitogen mount with krytox oil, and the crystals were optically aligned on a Bruker D8 Quest X-ray diffractometer using a built-in camera. Preliminary measurements were performed using an I- μ -S X-ray source (Mo $K\alpha$, $\lambda = 0.71073 \text{ \AA}$) with high-brilliance and high-performance focusing quest multilayer optics. Data were collected, reflections were indexed and processed, and the files were scaled and corrected for absorption using APEX2.²¹ The reflection's intensities of a sphere were collected by a mixture of four sets of frames. Each set had a different omega angle for the crystal, and each exposure covered a range of 0.50 in ω , totaling to 1464 frames. The frames were collected with an exposure time of 5–25 s which was dependent on the crystal. SAINT software was used for data integration including polarization and Lorentz corrections.²⁴ The files were scaled and corrected for absorption using SADABS.²¹ The space groups were assigned, and the structures were solved by direct methods using XPREP within the SHELXTL suite of programs^{22,23} and refined by full matrix least-squares against F^2 with all reflections using Shelxl2016 or 2017²⁹ using the graphical interface Shelxle.²⁵ Structure factors for Bk, Am, and Cf were not defined in the Shelxl software and were manually defined using the values published in the International tables of Crystallography, Vol. C, Tables 4.2.6.8 (entries a1 to c of the scattering factor line), 6.1.1.4 (f' and f''), and 4.2.4.2 (μ).^{29,30} For the atomic weight, the value of the actual isotope was used (not necessarily that of the longest lived isotope). The structures of Am and Bk are isomorphous and were refined against a common model. Neither exhibits any disorder. In the Cf structure, one of the DOPO ligands undergoes a rotating motion around californium. It was refined as disordered over two orientations. Both moieties were restrained to have a similar geometry as the second nondisordered DOPO ligand. Atoms C49 and C49B were constrained to have identical ADPs. A pyridine solvate molecule is disordered around an inversion center. Another pyridine solvate molecule is disordered in a general position. A third pyridine solvate molecule was refined as partially occupied. Ill-defined diffuse electron density around the first and third pyridine molecules could not be assigned to any additional solvate molecules and was ignored in the structural model (it might be the cause for partial occupancy of the third pyridine molecule). U^{ij} components of all disordered atoms were restrained to be similar for atoms closer to each other than 1.7 Å. Subject to these conditions the occupancy ratios for the DOPO moieties refined to 0.522(13) to 0.478(13). That of the disordered pyridine refined to 0.584(12) to

0.416(12). The occupancy rate for the partially occupied pyridine molecule refined to 0.707(5).

Magnetometry. Magnetic data for lanthanides were collected on a Quantum Design Magnetic Property Measurement System (MPMS-7). Temperature-dependent data were collected under applied 1 T DC fields from 2 to 300 K, and field dependent data were collected at 2 K with varying applied magnetic field strengths ranging from 0 to 7 T. Corrections for the intrinsic diamagnetism of the samples were made using Pascal's constants.³¹

Each magnetism sample was prepared in the glovebox and placed in a heat-sealed compartment of a plastic drinking straw. The plastic drinking straws were evacuated overnight prior to use. These straws were then sealed at one end ($\sim 9.5 \text{ cm}$ from the top) by heating a pair of forceps and crimping the sides of the straw until the two sides were fused together. The microcrystalline compound (10–40 mg) was loaded into the straw, capped with $<10 \text{ mg}$ of quartz wool (dried at $250 \text{ }^\circ\text{C}$ prior to use), and packed in tightly using a Q-tip. The other end of the plastic drinking straw was then sealed directly above the quartz wool, forming a small compartment ($<1 \text{ cm}$). The sample and quartz wool were massed four times each to the nearest 0.1 mg, and the values used were the averages of these mass measurements.

Computational Methods. Geometry optimizations were performed for a model Metal-DOPO complex (in which the *t*-Bu groups have been replaced with hydrogen atoms), for the maximum spin multiplicity with unrestricted density functional theory (UDFT) as implemented in the ADF2016 software package,^{32–34} employing the hybrid B3LYP functional^{35,36} in combination with the UFF dispersion corrections.³⁷ A TZP quality basis was used for the lanthanide or actinide, while a DZP quality basis was employed for the other atoms (H, C, O, N). Scalar relativistic effects were included by means of the zeroth order regular approximation (ZORA) to the Dirac equation.^{38,39} This methodology is termed UDFT-B3LYP-UFF-ZORA, or UDFT-ZORA or DFT for simplicity. The electronic structures were analyzed with complete active Space SCF (CASSCF) calculations on top of the DFT optimized structures using the Molcas 8.2 software package.⁴⁰ Small-core relativistic effective core potentials (ECP) of the Stuttgart-Cologne group were applied for all elements,^{41,42} along with segmented basis sets^{43–45} for lanthanides with the following contraction (14s, 13p, 10d, 8f, 6g)/[10s, 8p, 5d, 4f, 3g], the following contraction for actinides (14s, 13p, 10d, 8f, 6g)/[10s, 9p, 5d, 4f, 3g], the following contraction for N and C (4s, 4p)/[2s, 2p], the following contraction for oxygen (4s, 5p)/[2s, 3p], and the following contraction for hydrogen (4s)/[4s]. Resolution of identity Cholesky decomposition (RICD)⁴⁶ was used for reducing the computational cost of computing the two-electron integrals.

Preparation of $\text{Ce}(\text{DOPO}^{\text{q}})_3$. A 20 mL scintillation vial was charged with anhydrous CeCl_3 (0.028 g, 0.114 mmol) and 5 mL of pyridine. To this suspension was added a violet solution of HDOPO^{q} (0.150 g, 0.343 mmol) in 5 mL of pyridine, resulting in an immediate color change to dark blue. After stirring for 2 h, the resulting solution was concentrated *in vacuo* to a dark blue powder. The product was extracted into 20 mL of pentane, and the solution was filtered to remove the pyridinium chloride byproduct. This solution was concentrated *in vacuo*, resulting in a blue powder assigned as $\text{Ce}(\text{DOPO}^{\text{q}})_3$ (0.126 g, 0.087 mmol, 76%). Suitable crystals for X-ray crystallography were grown from a concentrated solution of pentane at $-35 \text{ }^\circ\text{C}$ (^1H NMR (C_6D_6 , $25 \text{ }^\circ\text{C}$): $\delta = 0.69$ (3, 54H, $-\text{C}(\text{CH}_3)_3$), 1.92 (2, 54H, $-\text{C}(\text{CH}_3)_3$), 8.64 (2, 6H, Ar-CH).

Preparation of $\text{Nd}(\text{DOPO}^{\text{q}})_3$. A 20 mL scintillation vial was charged with anhydrous NdCl_3 (0.029 g, 0.116 mmol) and 5 mL of pyridine. To this suspension was added a violet solution of HDOPO^{q} (0.150 g, 0.343 mmol) in 5 mL of pyridine, resulting in an immediate color change to dark blue. After stirring for 2 h, the resulting solution was concentrated *in vacuo* to a dark blue powder. The product was extracted into 20 mL of pentane, and the solution was filtered to remove the pyridinium chloride byproduct. This solution was concentrated *in vacuo*, resulting in a blue powder assigned as $\text{Nd}(\text{DOPO}^{\text{q}})_3$ (0.112 g, 0.077 mmol, 68%). Suitable crystals for X-ray crystallography were grown from a concentrated solution of pyridine.

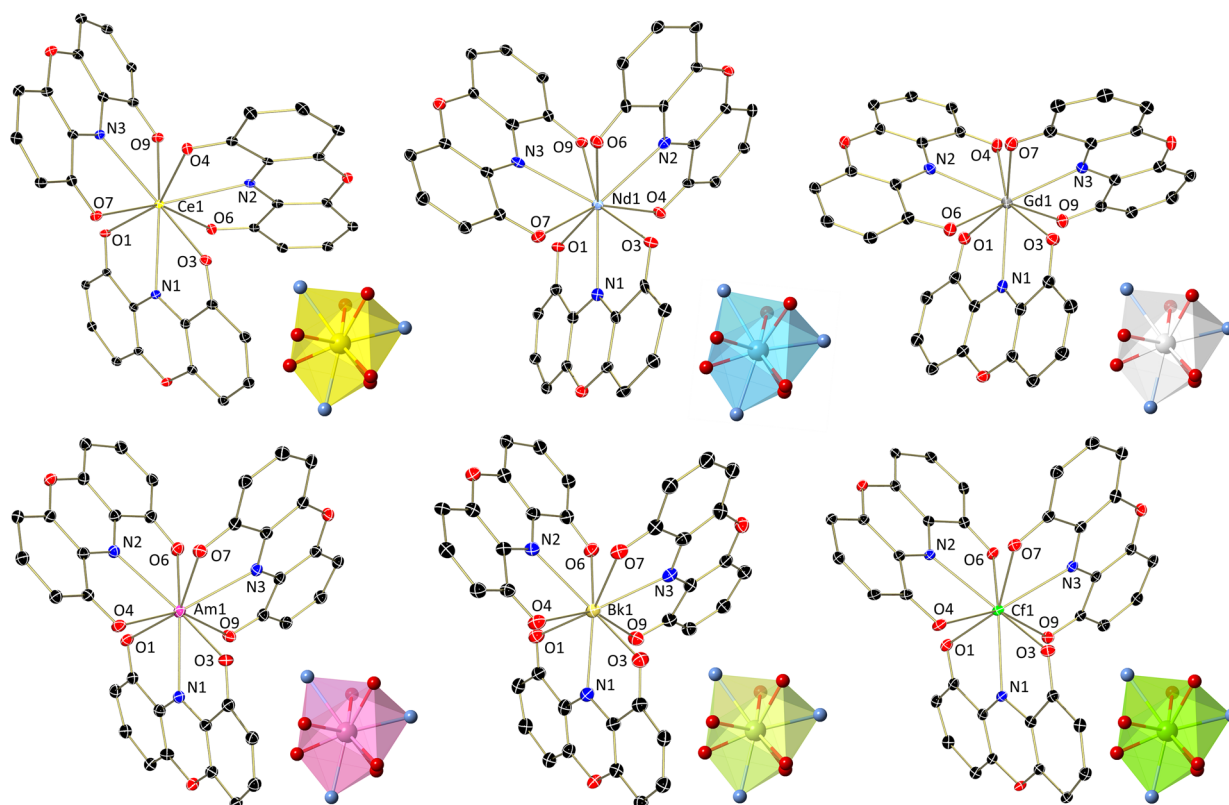


Figure 1. Molecular structures of $\text{Ce}(\text{DOPO})_3$, $\text{Nd}(\text{DOPO})_3$, $\text{Gd}(\text{DOPO})_3$, $\text{Am}(\text{DOPO})_3$, $\text{Bk}(\text{DOPO})_3$, and $\text{Cf}(\text{DOPO})_3$ shown at 30% probability ellipsoids. Hydrogen atoms, *tert*-butyl groups, and cocrystallized solvent molecules have been omitted for clarity. These data represent a unique isostructural series from representatives through the entire *f*-block. Average metrical oxidation states¹¹ for each compound support the formulation of each ligand as the monoanionic, DOPO[−] resonance form: $\text{Ce}(\text{DOPO})_3$, −1.08(15); $\text{Nd}(\text{DOPO})_3$, −1.03(15); $\text{Gd}(\text{DOPO})_3$, −1.13(13); $\text{Am}(\text{DOPO})_3$, −1.08(14); $\text{Bk}(\text{DOPO})_3$, −1.08(12); $\text{Cf}(\text{DOPO})_3$, −1.08(14).

¹H NMR (C_6D_6 , 25 °C): δ = 1.03 (6, 54H, $-\text{C}(\text{CH}_3)_3$), 1.84 (3, 54H, $-\text{C}(\text{CH}_3)_3$), 9.09 (4, 6H, Ar–CH).

Preparation of $\text{Sm}(\text{DOPO})_3$. A 20 mL scintillation vial was charged with anhydrous SmCl_3 (0.030 g, 0.114 mmol) and 5 mL of pyridine. To this suspension was added a violet solution of HDOPO[−] (0.150 g, 0.343 mmol) in 5 mL of pyridine, resulting in a color change to dark blue after 5 min. After stirring for 2 h, the resulting solution was concentrated *in vacuo* to a dark blue powder. The product was extracted into 20 mL of pentane, and the solution was filtered to remove the pyridinium chloride byproduct. This solution was concentrated *in vacuo*, resulting in a blue powder assigned as $\text{Sm}(\text{DOPO})_3$ (0.124 g, 0.084 mmol, 74%). Suitable crystals for X-ray crystallography were grown from a concentrated solution of pyridine. Paramagnetism of the sample precluded analysis by ¹H NMR spectroscopy.

Preparation of $\text{Gd}(\text{DOPO})_3$. A 20 mL scintillation vial was charged with anhydrous GdCl_3 (0.030 g, 0.114 mmol) and 5 mL of pyridine. To this suspension was added a violet solution of HDOPO[−] (0.150 g, 0.343 mmol) in 5 mL of pyridine, resulting in a color change to dark blue after 5 min. After stirring for 2 h, the resulting solution was concentrated *in vacuo* to a dark blue powder. The product was extracted into 20 mL of pentane, and the solution was filtered to remove the pyridinium chloride byproduct. This solution was concentrated *in vacuo*, resulting in a blue powder assigned as $\text{Gd}(\text{DOPO})_3$ (0.119 g, 0.081 mmol, 71%). Suitable crystals for X-ray crystallography were grown from a concentrated solution of pyridine. Paramagnetism of the sample precluded analysis by ¹H NMR spectroscopy.

Preparation of $\text{Am}(\text{DOPO})_3$. A 7 mL scintillation vial was charged with ²⁴³AmBr₃ (0.005 g, 0.0104 mmol) and 2 mL of pyridine. A violet solution of HDOPO[−] (0.0135 g, 0.0311 mmol) dissolved in 2 mL of pyridine was added to the vial, causing a color change from

yellow to dark purple. The solution sat overnight to allow evaporation of solvent. Dark purple block crystals suitable for X-ray analysis formed and were analyzed immediately.

Preparation of $\text{Bk}(\text{DOPO})_3$. A 7 mL scintillation vial was charged with ²⁴⁹BkCl₃ (4.33 mg, 0.014 mmol) and 1 mL of pyridine. A violet solution of HDOPO[−] (19.2 mg, 0.043 mmol) and 1 mL of anhydrous pyridine was added to the vial, causing a color change from green to blue. The solution was dried to a residue, and 10 equiv of HDOPO[−] (61.2 mg, 0.140 mmol) in 1 mL of pyridine were added. The solution was transferred to a 20 mL scintillation vial via pasteur pipette. Upon standing blue rod crystals suitable for X-ray analysis formed.

Preparation of $\text{Cf}(\text{DOPO})_3$. A 20 mL scintillation vial was charged with ²⁴⁹CfCl₃ (5 mg, 0.014 mmol) and 1 mL of pyridine. A violet solution of HDOPO[−] (61.2 mg, 0.140 mmol) in 1 mL of anhydrous pyridine was added to the vial, causing a color change from green to blue. The solution was dried to a residue, and the product was extracted with 1 mL of pentane. The blue pentane solution was transferred to a 20 mL scintillation vial and dried. The residue was then redissolved in 1 mL of pyridine. Upon standing, dark blue platelet crystals suitable for X-ray analysis formed.

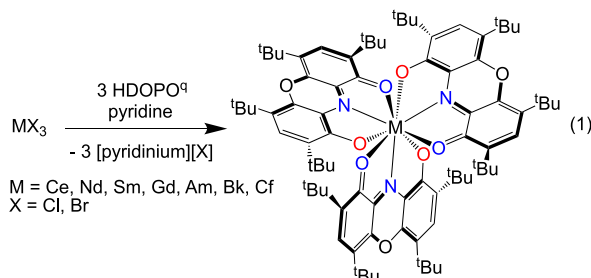
RESULTS AND DISCUSSION

Synthesis of Lanthanide Compounds. Initial synthetic efforts focused on the synthesis of lanthanide tris(ligand) derivatives that would serve as model compounds for transuranium elements. An efficient synthesis using high boiling solvents that would quickly and reliably yield the desired tris(ligand) complexes was required for eventual extension to the appropriate transuranium materials. Treating stirring pyridine solutions of either CeCl_3 , NdCl_3 , SmCl_3 , or

Table 1. Metal–Ligand Bond Distances (in Å) for Ln/An DOPO Complexes

	Ce(DOPO ^q) ₃	Nd(DOPO ^q) ₃	Gd(DOPO ^q) ₃	Am(DOPO ^q) ₃	Bk(DOPO ^q) ₃	Cf(DOPO ^q) ₃
M-O1	2.4825(19)	2.489(3)	2.4484(16)	2.488(3)	2.459(4)	2.448(2)
M-N1	2.644(2)	2.570(4)	2.5426(19)	2.554(3)	2.522(4)	2.511(2)
M-O3	2.5204(19)	2.463(3)	2.4276(17)	2.463(3)	2.436(3)	2.423(2)
M-O4	2.5234(18)	2.492(3)	2.4514(15)	2.493(3)	2.468(3)	2.463(2)
M-N2	2.653(2)	2.608(4)	2.5527(19)	2.591(3)	2.571(4)	2.549(2)
M-O6	2.5058(19)	2.470(3)	2.4295(16)	2.474(3)	2.454(3)	2.436(2)
M-O7	2.5073(17)	2.474(3)	2.4316(17)	2.482(3)	2.452(3)	2.456(2)
M-N3	2.634(2)	2.587(4)	2.514(2)	2.582(3)	2.544(4)	2.538(2)
M-O9	2.4934(19)	2.473(3)	2.4206(15)	2.472(3)	2.447(3)	2.435(2)

GdCl₃ with 3 equiv of HDOPO^q generated deep blue solutions in each case, indicative of ligand metalation (eq 1). Removal of the volatiles *in vacuo* followed by trituration with pentane and filtration to remove pyridinium chloride produced the corresponding tris(ligand) products, Ln(DOPO^q)₃ (Ln = Ce, Nd, Sm, Gd) as teal blue solids in good yields (76%, 68%, 74%, and 71% respectively). Analysis by ¹H NMR spectroscopy of Gd(DOPO^q)₃ was not possible due to the paramagnetism stemming from the 7 unpaired electrons of Gd(III), but the Ce(III), f¹ and Nd(III), f³ analogues produced interpretable spectra that had the appropriate number of peaks consistent with the expected symmetry of Ln(DOPO^q)₃ (Ln = Ce, Nd) (Figures S1–S2).



Crystallization of Ce(DOPO^q)₃, Nd(DOPO^q)₃, Sm(DOPO^q)₃, and Gd(DOPO^q)₃ was possible directly from small scale mixtures utilizing 10 mg of LnCl₃, 3 equiv of ligand, and 5 mL of pyridine. Slow evaporation over 24 h caused blue crystals to reliably and reproducibly precipitate from these concentrated solutions. Analysis of the crystals by X-ray diffraction confirmed the identities as Ce(DOPO^q)₃, Nd(DOPO^q)₃, Sm(DOPO^q)₃, and Gd(DOPO^q)₃,^{17,18} and the molecular structures of Ce, Nd, and Gd are presented in Figure 1 (metrical parameters displayed in Table 1). In all cases, three statistically indistinguishable DOPO ligands were observed. The M–O distances in ranges of 2.4825(19)–2.5234(18) Å for Ce(DOPO^q)₃, 2.463(3)–2.492(3) Å for Nd(DOPO^q)₃, 2.4435(15)–2.4721(15) Å for Sm(DOPO^q)₃, and 2.4206(15)–2.4514(15) Å for Gd(DOPO^q)₃ are all appropriate for formulation as monoanionic quinone ligands. In this resonance form, the M–O bond distances should be averaged, as one bond has anionic character while the other is dative. Both the DOPO^q and DOPO^{cat} forms of the ligand would display shorter bond distances because there would be no dative M–O interactions. Furthermore, the M–N distances are all long, with average values of 2.644, 2.588, 2.5654, and 2.536 Å for

Ce(DOPO^q)₃, Nd(DOPO^q)₃, Sm(DOPO^q)₃, and Gd(DOPO^q)₃, respectively, again pointing toward the DOPO^q resonance form, which features a dative M–N interaction. Because structural parameters are useful in assigning ligand oxidation states, analysis of the intraligand metrical parameters for each molecular structure were studied using the Metrical Oxidation State (MOS) method previously established by Brown.¹¹ Using this model, which takes into account the errors associated with crystallographic determinations, the average ligand oxidation states were calculated. The average values of –1.08(15) (Ce(DOPO^q)₃), –1.03(15) (Nd(DOPO^q)₃), –1.26(23) (Sm(DOPO^q)₃), and –1.13(13) (Gd(DOPO^q)₃) are all consistent with the monoanionic, quinone resonance form of the ligand (Tables S2–S5). By charge balance considerations, each lanthanide ion would be in the formal +3 oxidation state, as expected based on the typical valency of these metals.

Further confirmation of the ligand oxidation states for Ce(DOPO^q)₃, Nd(DOPO^q)₃, Sm(DOPO^q)₃, and Gd(DOPO^q)₃ was obtained from electronic absorption spectroscopic measurements (Figure 2). With experimental constraints for transuranic compounds in mind, the data for the lanthanide species were collected in the range 300–1000 nm on single crystal samples. The data for each lanthanide derivative are analogous, showing two pronounced features in the visible region, with absorbances appearing at 399 and 716 nm for Ce(DOPO^q)₃, at 403 and 731 nm for Nd(DOPO^q)₃, at 403 and 723 nm for Sm(DOPO^q)₃, and at 401 and 716 nm for Gd(DOPO^q)₃. The quinone form of the ligand typically shows intense ligand-to-metal charge-transfer bands in the 650–800 nm range due to transitions into an empty DOPO^q-based π^* orbital. The data for Ce(DOPO^q)₃, Nd(DOPO^q)₃, Sm(DOPO^q)₃, and Gd(DOPO^q)₃ are in accord with the uranium derivative, UO₂(DOPO^q)₂ ($\lambda_{\text{max}} = 719$ nm, 14,400 cm^{–1} M^{–1}),¹⁶ as well as the alkali metal ligand salts KDOPO^q(THF) ($\lambda_{\text{max}} = 735$ nm, 9750 cm^{–1} M^{–1})¹⁶ and NaDOPO^q ($\lambda_{\text{max}} = 695$ nm).¹⁵ The intensity of these ligand based transitions are such that any features from the lanthanide ion are dwarfed.

To further support the ground state electronic structures in Ln(DOPO^q)₃ (Ln = Ce, Nd, and Gd), variable temperature magnetization and field-dependent magnetic measurements were performed (Figure 3). At room temperature, the μ_{eff} values of Ce(DOPO^q)₃, Nd(DOPO^q)₃, and Gd(DOPO^q)₃ were 2.49, 3.61, and 7.90 μ_{B} , respectively, in good agreement with the expected magnetic moments, 2.53, 3.62, and 7.94 μ_{B}

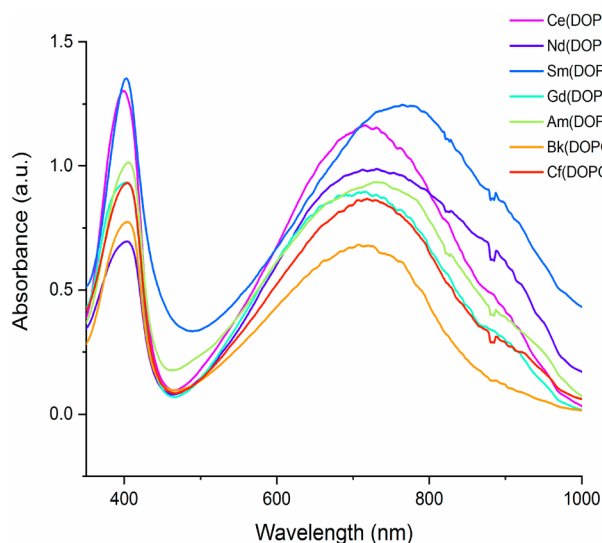


Figure 2. Electronic absorption spectra for $\text{Ce}(\text{DOPO}^q)_3$, $\text{Nd}(\text{DOPO}^q)_3$, $\text{Sm}(\text{DOPO}^q)_3$, $\text{Gd}(\text{DOPO}^q)_3$, $\text{Am}(\text{DOPO}^q)_3$, $\text{Bk}(\text{DOPO}^q)_3$, and $\text{Cf}(\text{DOPO}^q)_3$ presented as absorbance. Data were collected on single crystals at ambient temperature in the range 300–1000 nm. Each compound shows two strong absorbances in the ranges 398–405 nm and 706–732 nm assignable to charge transfer bands for the ligand π to π^* transitions. The intensity of these absorptions supports the formulation that all ligands are in the monoanionic, DOPO^q form, as electronic transitions to the low-lying empty π^* orbitals of the ligands are spin allowed.

for Ce^{3+} , Nd^{3+} , and Gd^{3+} cations.^{17,46–52} Upon cooling, the μ_{eff} values decreased to 1.23, 1.97, and $6.49 \mu_{\text{B}}$, respectively, at 2 K. Such decreases in moments at lower temperatures for $\text{Ce}(\text{DOPO}^q)_3$ and $\text{Nd}(\text{DOPO}^q)_3$ results from the depopulation of Stark energy levels created by crystal field perturbations of the $J = 5/2$ and $J = 9/2$ manifold for the respective Ce^{3+} and Nd^{3+} cations. The behavior of $\text{Gd}(\text{DOPO}^q)_3$ was consistent with that previously reported.¹³ Overall the magnetic data are consistent with monoanionic ligands that are in their quinone states ($S = 0$); the magnetic responses of the $\text{Ln}(\text{DOPO}^q)_3$ complexes arise solely from the paramagnetic Ln^{3+} cations, with no open shell ligand contributions.

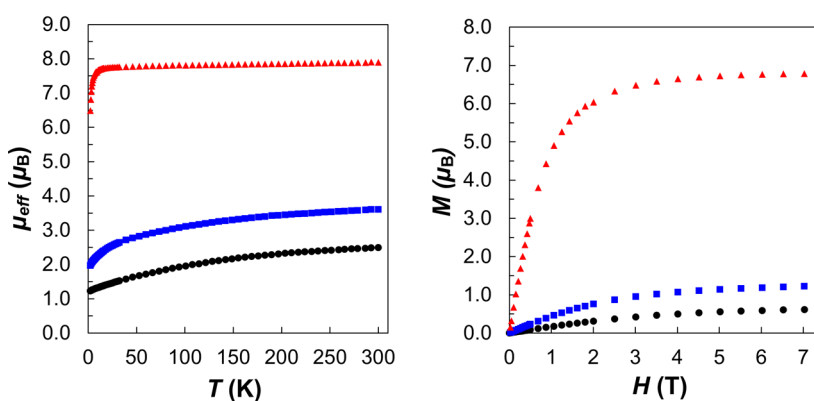


Figure 3. Variable-temperature molar magnetic data (μ_{eff}) for $\text{Ce}(\text{DOPO}^q)_3$ (black, \bullet), $\text{Nd}(\text{DOPO}^q)_3$ (blue, \blacksquare), and $\text{Gd}(\text{DOPO}^q)_3$ (red, \blacktriangle) (left). The high temperature magnetic moments of 2.49, 3.61, and $7.90 \mu_{\text{B}}$ for $\text{Ce}(\text{DOPO}^q)_3$, $\text{Nd}(\text{DOPO}^q)_3$, and $\text{Gd}(\text{DOPO}^q)_3$, respectively, are in good agreement with the calculated magnetic moments, 2.53, 3.62, and $7.94 \mu_{\text{B}}$ for Ce^{3+} , Nd^{3+} , and Gd^{3+} cations. These data confirm that all three lanthanides are trivalent, and each cation is supported by three monoanionic DOPO^q ligands. Variable field data collected at 2 K are also presented (right). These data are consistent with the expectations for the ground state magnetization in each case.

Synthesis of Actinide Compounds. With the synthetic and crystallization procedures established for the lanthanides, these protocols were scaled to perform on 5 mg quantities of halide salts in preparation for extension to transuranium elements, including americium, berkelium, and californium. As for the lanthanide models, mixing $^{243}\text{AmBr}_3$ and HDOPO resulted in the formation of $\text{Am}(\text{DOPO}^q)_3$. Due to the technical challenges associated with transuranium elements, characterization by ^1H NMR spectroscopy was not possible. However, analysis of single crystals obtained from the analogous crystallization conditions confirmed the molecular structure of $\text{Am}(\text{DOPO}^q)_3$. In this case, the americium has three DOPO^q ligands chelated to form a 9-coordinate distorted tricapped trigonal prismatic geometry (structure in Figure 1; bond metrics in Table 1). The $\text{Am}-\text{O}$ distances range from 2.463(3) to 2.494(3) Å, as the anionic and dative interactions are averaged across each ligand. For comparison, pure dative $\text{Am}-\text{O}$ interactions range from 2.508(6) to 2.525(4) Å in $[\text{Am}(\text{TMOGA})_3][\text{ClO}_4]_3$ (TMOGA = tetramethyl-3-oxa-glutaramide).⁵³ No purely anionic $\text{Am}-\text{O}$ bonds were noted in the CSD. The $\text{Am}-\text{N}$ bond distances range from 2.545(3) to 2.591(3) Å and are on par with those observed for $[\text{Am}(\text{PDA})(\text{NO}_3)(\text{H}_2\text{O})_2]\cdot\text{H}_2\text{O}$ ⁵⁴ (H_2PDA = 1,10-phenanthroline-2,9-dicarboxylic acid) of 2.589(11) Å and $\text{Am}(\text{HDPa})_3$ ¹¹ of (2.551(4), 2.591(3), 2.550(4)) Å, both of which are established as containing Am^{III} . The intraligand $\text{C}-\text{O}$ bonds range from 1.265(5) to 1.276(5) Å and $\text{C}-\text{N}$ bonds range from 1.321(5) to 1.342(5) Å, producing an average MOS value of $-1.08(14)$ for the ligands (Table S5). These intraligand bond metrics are in correspondence with published DOPO^q distances for transition metals.

With the successful synthesis of $\text{Am}(\text{DOPO}^q)_3$, the berkelium and californium variants, $\text{Bk}(\text{DOPO}^q)_3$ and $\text{Cf}(\text{DOPO}^q)_3$, were also targeted. Treating either $^{249}\text{BkCl}_3$ or $^{249}\text{CfCl}_3$ with 3 equiv of HDOPO in pyridine produced the same striking color change from pale green to vibrant teal, indicative of the desired products. Furthermore, using 10 equiv of ligand instead of 3 equiv aided in crystallization; thus, single crystals suitable for X-ray diffraction could be isolated within 1 h. In the absence of excess ligand, the time scale of crystallization was too long, and radiolytic degradation of

Table 2. DFT Computed (and Difference with Experiment in Brackets) Metal–Ligand Bond Distances (in Å) for Ln/An DOPO Complexes^a

	Ce(DOPO ^q) ₃	Nd(DOPO ^q) ₃	Gd(DOPO ^q) ₃	Am(DOPO ^q) ₃	Bk(DOPO ^q) ₃	Cf(DOPO ^q) ₃
M-O1	2.512 (0.030)	2.527 (0.064)	2.476 (0.048)	2.586 (0.098)	2.505 (0.046)	2.545 (0.097)
M-N1	2.553 (-0.091)	2.557 (-0.013)	2.495 (-0.048)	2.542 (-0.012)	2.441 (-0.081)	2.494 (-0.017)
M-O3	2.515 (-0.005)	2.520 (0.031)	2.477 (0.029)	2.595 (0.132)	2.495 (0.059)	2.537 (0.114)
M-O4	2.533 (0.027)	2.518 (0.026)	2.474 (0.023)	2.579 (0.086)	2.590 (0.112)	2.567 (0.104)
M-N2	2.577 (-0.076)	2.554 (-0.054)	2.494 (-0.059)	2.522 (-0.069)	2.494 (-0.077)	2.492 (-0.057)
M-O6	2.530 (0.007)	2.529 (0.059)	2.477 (0.047)	2.586 (0.112)	2.528 (0.074)	2.528 (0.092)
M-O7	2.530 (0.023)	2.528 (0.055)	2.474 (0.042)	2.558 (0.086)	2.532 (0.085)	2.567 (0.132)
M-N3	2.571 (-0.063)	2.558 (-0.029)	2.493 (-0.021)	2.507 (-0.075)	2.492 (-0.052)	2.484 (-0.054)
M-O9	2.521 (0.028)	2.522 (0.048)	2.472 (0.051)	2.573 (0.091)	2.583 (0.131)	2.542 (0.086)

^aDFT calculation with B3LYP functional (with UFF dispersion) and DZP (TZP for Ln/An) basis set.

both desired compounds was observed as signified by a color change from teal to red-brown.

Overall, both the Bk–ligand and Cf–ligand bond distances are in accord with trivalent metals, as expected (structure in Figure 1; bond metrics in Table 1). In the berkelium and californium analogues, the Bk–O distances, ranging from 2.436(3) to 2.468(3) Å, and the Cf–O bond lengths, ranging from 2.423(2) to 2.463(2) Å, are within error of those reported for Bk(HDPA)₃ (2.410(3)–2.497(3) Å) and Cf(HDPA)₃ (2.387(4)–2.494(4) Å),¹¹ respectively. The long Bk–N (2.522(4), 2.571(4), and 2.544(4) Å) and Cf–N (2.511(2), 2.549(2), and 2.538(2) Å) distances are indicative of dative Bk–N and Cf–N interactions, suggesting central berkelium +3 and californium +3 ions, similar to those in Bk(HDPA)₃ and Cf(HDPA)₃. This is further supported by the intraligand distance analysis that yields nearly identical average MOS values of –1.08(12) for Bk(DOPO^q)₃ and –1.08(13) Å for Cf(DOPO^q)₃, supporting the monoanionic, quinone resonance form of the ligands is dominant in both cases (Tables S6–S7).

Characterization by electronic absorption spectroscopy on single crystals of Am(DOPO^q)₃, Bk(DOPO^q)₃, and Cf(DOPO^q)₃ further corroborates the formulation of the ligands as the monoanionic, DOPO^q resonance form (Figure 2). Again, these data show absorbances for π to π^* transitions for Am(DOPO^q)₃ at 427 and 746 nm, for Bk(DOPO^q)₃ at 404 and 707 nm, and for Cf(DOPO^q)₃ at 404 and 719 nm, which are all in accord with the lanthanide models. These ligand-based transitions are so intense that any features due to the individual metal ions are not visible. This analysis supports the similar teal-blue color that is noted for all of these complexes.

Computational Analysis. We optimized the structures of the Ln/An DOPO complexes using density functional theory

(DFT) with the B3LYP exchange correlation functional (in combination with UFF dispersion) and DZP (TZP for Ln or An) basis set. In Table 2 we reported the DFT metal–ligand bond distances along with the difference from the experimental values. The DFT metal–ligand bond lengths are similar to the experimental ones, even if DFT yields systematically shorter M–N bonds and longer M–O bonds. The highest deviations with respect to experiment are found for the actinides, which are about ± 0.1 Å. Overall the agreement is satisfactory, but because 0.1 Å of difference with experimental bond distances may produce sizable changes in bonding pattern, we decided to perform the computations using experimental geometries as well (vide infra).

In order to gain further insight into the bonding nature of the aforementioned synthesized compounds, we performed a computational analysis by means of complete active space self-consistent field (CASSCF) calculations, using DFT optimized geometries (see Computational Methods for details). Initial analysis started with the lanthanide–DOPO complexes: (Ce(III), Nd(III), Gd(III), and Sm(III)). For Ce(DOPO^q)₃, there is only one unpaired electron on the seven 4f orbitals, and therefore there is only one possible spin state, a doublet. The orbitals of the active space are shown in Figure S3. A LoProp⁵⁵ charge analysis and Mulliken spin density analysis were performed, Table S9, and, together with the orbital picture, they show that the orbitals and spin density are completely localized on the cerium (4f orbitals), with no interaction with the ligand. The latter are a way to estimate the atomic spin densities and therefore can provide insights in assigning the oxidation state of the metal and determining if there is any spin density contribution from the ligand, namely if the ligand is not in a closed shell state. The LoProp charges are a way to estimate the atomic charges and, in conjunction

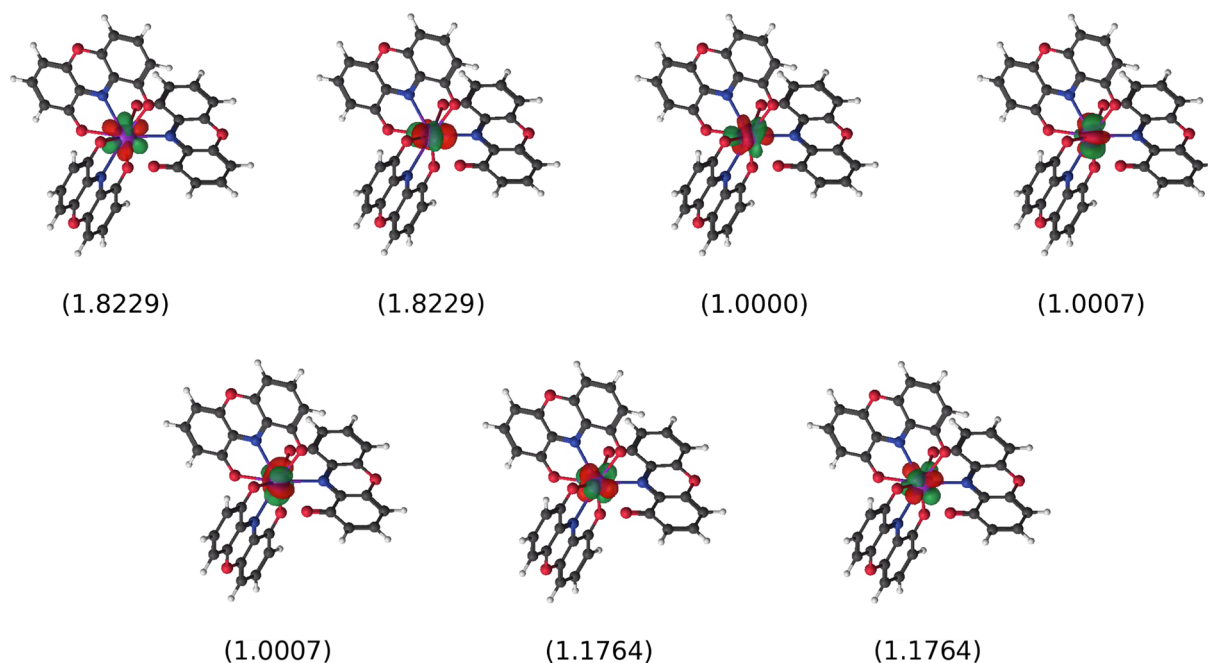


Figure 4. Active space orbitals (occupation numbers in brackets) for the ground state (sextet spin state) of $\text{Cf}(\text{DOPO}^{\text{q}})_3$.

with the previously mentioned spin density, can give further insights on the assignment of oxidation states and on the evaluation of charge accumulation or depletion in an atom (e.g., a metal) upon bonding (e.g., with a ligand). The LoProp charge for cerium is 2.54. In order to unveil possible ligand involvement, we expanded the active space by including two occupied (and the two corresponding virtual) orbitals on the ligands, corresponding to a CASSCF(5,11), namely 5 electrons in 11 orbitals. This calculation did not modify the spin density and LoProp charge on Ce, showing no electron delocalization between the Ce *f* orbitals and ligand orbitals (Table S11 and Figure S4).

The computational analysis for both Nd(III) (Tables S12–S13, Figure S5) and Gd(III) (Tables S14–S15, Figure S6) shows analogous results as the one for Ce(III). The wave function of the quartet ground state for Nd(III) has some multireference character, with a percentage of the dominant configuration of 89%. For Gd(III), we also expanded the active space performing a CASSCF(11,11), adding two ligand based orbitals (and the corresponding virtual orbitals); this calculation showed no electron delocalization between the Gd *f* orbitals and ligand orbitals (Tables S16–S17 and Figure S7). Regarding Sm(III), in Tables S18–S19 we can see that the ground state is the sextet spin state, where the wave function of the sextet ground state has multireference character, with a percentage of the dominant configuration of 58%. All the spin density is localized on Sm, with no electron delocalization on the ligands (active space orbitals shown in Figure S8). Thus, for the lanthanide–DOPO complexes, the computational analysis reveals no significant interaction between the metal and the ligands in terms of redox flexibility, in agreement with the experimental results.

Subsequently, CASSCF calculations were also performed for the actinide–DOPO analogues: Am(III), Bk(III), Cf(III). The $\text{Am}(\text{DOPO}^{\text{q}})_3$ complex presents an electronic structure with six unpaired electrons in seven 5*f* orbitals, CASSCF(6,7), allowing analysis in all possible spin states (septets, quintets, triplets, and singlets). The high-spin septet state was

determined to be the ground state (see Table S20). The orbitals for the septet ground state reveal a high localization of the unpaired electrons on the 5*f* orbitals of americium (Figure S9). Such localization has previously been found in related uranium(III)⁵⁶ and plutonium(III) complexes.⁵⁷ The wave function analysis of the septet ground state reveals that all the spin density is located on the Am atom, which has a LoProp charge of 2.44 (see Table S21). No orbital delocalization between Am(III) and the DOPO ligand occurs.

The computational analysis for $\text{Bk}(\text{DOPO}^{\text{q}})_3$ showed a similar picture. In this case, 8 electrons were distributed among the 7 5*f* orbitals, CASSCF(8,7). The highest spin state is the most stable one. The LoProp charge for Bk is 2.43, very similar to that for Am($\text{DOPO}^{\text{q}})_3$, and the spin density is 5.98. Overall, the active space orbitals are localized on berkelium(III), and there is no orbital interaction between Bk and the DOPO ligands (Tables S22–S23, Figure S10).

We also analyzed $\text{Cf}(\text{DOPO}^{\text{q}})_3$, by means of CASSCF(9,7) calculations for the sextet, quartet, and doublet spin states. Also, in this case, the ground state is the highest spin one, namely the sextet, with the quartet and doublet state being high in energy (see Tables S24–S25). The wave function analysis reveals a sizable multireference character. The spin density is all located on californium, with no orbital interaction with the ligands. Furthermore, the LoProp charge for Cf in the ground sextet state is 2.38, a bit smaller than the other complexes, but still pointing out to a Cf(III) oxidation state. The active space orbitals show that they are comprised of the Cf 5*f* electrons (Figure 4). For the Cf complex we also did a CASSCF(13,11) calculation including two orbitals on the ligands (and the two corresponding virtual orbitals) in the active space. The results of this analysis (Tables S26–S27 and Figure S12) show no ligand involvement, with all the spin localized on the californium atom.

From this computational analysis, we can conclude that the nature of the bonding of lanthanides and actinides with DOPO is analogous. Inspection of the SOMO levels for these complexes shows that these orbitals are entirely *f* orbital

based, with little to no ligand redox activity, even when going to expanded active spaces. In order to provide a quantitative picture of the bonding, we also analyzed the percentage of contribution of the orbitals composing the active space for Cf and Sm complexes, using DFT optimized structures (Tables S29–S30). Quantitatively, we clearly see that the active space orbitals are composed only by *f* orbitals of Cf or Sm, with neither *d* contribution of Cf or Sm nor contributions from oxygen and nitrogen atoms bonded to them.

In order to verify if the geometrical differences between DFT and experimental (shown in Table 2) would produce any change in the bonding patterns, we performed the same aforementioned CASSCF analysis using experimental structures (in which we replaced the *t*-Bu groups with hydrogen atoms, and only the H positions have been optimized with DFT; see computational details). From Tables S31 to S50, we can see that we do not observe sizable changes in bonding pattern with respect to DFT optimized geometries.

With this rare isostructural family in hand, it is possible to now make comparisons of structural parameters across the actinide series. As periodic trends dictate, traversing the actinide series from left to right results in a decrease in atomic radius. Theory predicts in moving from Am to Cf that there should be a decrease by 0.01 Å with each step, for a total of a 0.03 Å decrease. Examination of the difference between the average Am–N (2.572(4) Å, 2.524 Å with DFT) and Cf–N (2.533(2) Å, 2.490 Å with DFT) bonds is $\Delta = 0.04$ Å (0.034 Å with DFT), while the difference in the respective bond distances for the corresponding M–O bonds (Am: 2.475(4), 2.580 Å with DFT; Cf: 2.444(2) Å, 2.548 Å with DFT) is $\Delta = 0.03$ Å (0.032 Å with DFT). Although the magnitude of the Δ value is as expected, these values differ from what has been previously established for californium. For instance, by comparing Am(Hdpa)₃ and Cf(Hdpa)₃, average values for $\Delta(\text{M–O}) = 0.046, 0.037$ Å and $\Delta(\text{M–N}) = 0.042, 0.037$ Å indicate that there is more contraction in these bonds as compared to the tris(DOPO)^q system. This is likely due to both steric and electronic factors, as the extreme sterics imparted by the rigid tris(DOPO)^q framework could result in slight bond elongation to alleviate strain.

The results presented here highlight important differences between metals in different areas of the periodic table. While transition metals ligated by redox-active ligands are established to be highly covalent, we do not observe this behavior for the lanthanides and actinides. This is perhaps not surprising in the former case, since lanthanides are known to form coordination compounds with purely ionic bonds. However, this is somewhat unexpected in the later actinide complexes, as recent studies point to a higher potential of this type of bonding manifold due to the accidental energy equivalency of the 5*f* orbitals with the 2*p* orbitals of the N and O linker atoms.

CONCLUDING REMARKS

For the first time, a nonaqueous isostructural series of coordination compounds has been developed for members across the lanthanide and actinide series. By combining expertise in nonaqueous synthetic techniques with the knowledge and ability to manipulate elements from all throughout the *f*-block, we have used dioxophenoxazine (DOPO) ligands to make the broadest nonaqueous series known. Structural analysis of these representatives reveals trends across the actinide series, which are supported by spectroscopic measurements and computational analyses.

Altogether, this combination of studies highlights the importance of blending synthesis, characterization, and computational techniques to contribute to the overall understanding of bonding between organic ligands and metals at the bottom of the periodic table.

From the computational point of view, the DFT metal–ligand bond lengths are similar to the experimental ones, even if the UDFT-ZORA yields systematically shorter M–N and longer M–O bonds. The highest deviations with respect to experiment are found for the actinides, which are about ± 0.1 Å. However, this difference from experimental bond distances did not produce changes in the bonding pattern; i.e., the same CASSCF analysis using experimental structures versus UDFT-ZORA optimized structures does not yield sizable changes in bonding patterns. This shows that UDFT-ZORA combined with CASSCF could be a useful first approximation to predict and investigate the structure and electronic properties of actinides that are difficult to synthesize or characterize.

Finally, the studies here establish trends in the periodic table for redox-active ligand complexes. Despite the fact that transition metal derivatives of this ligand class are typically highly covalent with a large extent of electron delocalization, this is not observed here for the later actinides. As shown through these structural, spectroscopic, and computational studies, the electrons here are localized purely on the actinide rather than the π^* orbitals of the ligand. The lack of covalency noted here is surprising, given the signs of this phenomenon in other late actinide compounds. The An(Hdpa)₃ (An = Am, Cm, Cf, Bk) family shows small degrees of covalency in the metal–ligand bonds, evident from structural characterization, as does the californium borate, Cf[B₆O₈(OH)₅].⁵⁸ Protein derived systems, such as a recently reported berkelium siderophore from Abergel, also display some degree of covalent bonding.⁵⁹ Future studies aim to expand this family to tetravalent actinides, which should engage the redox activity of these ligands further.

ASSOCIATED CONTENT

Supporting Information

The Supporting Information is available free of charge on the ACS Publications website at DOI: 10.1021/jacs.8b10251.

Spectroscopic data, metrical oxidation tables, and computational details (PDF)

Crystallographic data for Gd(DOPO^q)₃ (CIF)

Crystallographic data for Nd(DOPO^q)₃ (CIF)

Crystallographic data for Sm(DOPO^q)₃ (CIF)

Crystallographic data for Ce(DOPO^q)₃ (CIF)

Crystallographic data for Cf(DOPO^q)₃ (CIF)

Crystallographic data for Bk(DOPO^q)₃ (CIF)

Crystallographic data for Am(DOPO^q)₃ (CIF)

AUTHOR INFORMATION

Corresponding Author

*sbart@purdue.edu

ORCID

Carlo Alberto Gaggioli: 0000-0001-9105-8731

Yusen Qiao: 0000-0001-7654-8636

Matthias Zeller: 0000-0002-3305-852X

Srimanta Pakhira: 0000-0002-2488-300X

Jose L. Mendoza-Cortes: 0000-0001-5184-1406

Eric J. Schelter: 0000-0002-8143-6206

Thomas E. Albrecht-Schmitt: 0000-0002-2989-3311

Laura Gagliardi: 0000-0001-5227-1396

Suzanne C. Bart: 0000-0002-8918-9051

Notes

The authors declare no competing financial interest.

Crystallographic data for the structures reported in this paper have been deposited at the Cambridge Structural Database,⁶⁰ under the deposition numbers (Ce) 1587903, (Nd) 1587898, (Sm) 1865059, (Gd) 1587897, (Am) 1566690, (Bk) 1587881, and (Cf) 1587880. Copies of these data can be obtained free of charge via www.ccdc.cam.ac.uk/data_request/cif.

ACKNOWLEDGMENTS

This work was funded by the Division of Chemical Sciences, Geosciences, and Biosciences, Office of Basic Energy Sciences of the U.S. Department of Energy through Grants DE-SC0008479 (S.C.B.), USDOE/DE-SC002183 (L.G.), and DE-FG02-13ER16414 (T.E.A.S.). L.G. used resources of the National Energy Research Scientific Computing Center, a DOE Office of Science User Facility supported by the Office of Science of the U.S. Department of Energy under Contract No. DE-AC02-05CH11231. E.J.S. acknowledges the U.S. Department of Energy, Office of Science, Office of Basic Energy Sciences, Separation Science program under Award Number DE-SC0017259 for financial support. The X-ray diffractometer at Purdue University used in this study was funded by the National Science Foundation through the Major Research Instrumentation Program under Grant No. CHE 1625543. We thank Prof. Jay Kikkawa (UPenn Physics) for assistance with the magnetic measurements. J.L.M.-C. acknowledges support from the Energy and Materials Initiative at Florida State University (FSU). J.L.M.-C. thanks the High-Performance Computer cluster at the Research Computing Center (RCC) at FSU for providing computational resources and support.

REFERENCES

- (1) Nash, K. L.; Nilsson, M. Introduction to the reprocessing and recycling of spent nuclear fuels. In *Reprocessing and Recycling of Spent Nuclear Fuel*; Taylor, R., Ed.; Woodhead Publishing Ltd.: Philadelphia, PA, USA, 2015; Vol. 79, pp 3–25.
- (2) Herbst, R. S.; Baron, P.; Nilsson, M. *Advanced separation techniques for nuclear fuel reprocessing and radioactive waste treatment*; Elsevier: Cambridge, 2011.
- (3) Trumm, S.; Geist, A.; Panak, P. J.; Fanghanel, T. An improved hydrolytically-stable bis-triazinyl-pyridine (BTP) for selective actinide extraction. *Solvent Extr. Ion Exch.* **2011**, *29*, 213–229.
- (4) Lewis, F. W.; Harwood, L. M.; Hudson, M. J.; Drew, M. G. B.; Desreux, J. F.; Vidick, G.; Bouslimani, N.; Modolo, G.; Wilden, A.; Sypula, M.; Vu, T. H.; Simonin, J. P. Highly efficient separation of actinides from lanthanides by a phenanthroline-derived bis-triazine ligand. *J. Am. Chem. Soc.* **2011**, *133*, 13093–13102.
- (5) Panak, P. J.; Geist, A. Complexation and extraction of trivalent actinides and lanthanides by triazinylpyridine N-donor ligands. *Chem. Rev.* **2013**, *113*, 1199–1236.
- (6) Smith, D. A.; Beweries, T.; Blasius, C.; Jasim, N.; Nazir, R.; Nazir, S.; Robertson, C. C.; Whitwood, A. C.; Hunter, C. A.; Brammer, L.; Perutz, R. N. The contrasting character of early and late transition metal fluorides as hydrogen bond acceptors. *J. Am. Chem. Soc.* **2015**, *137*, 11820–11831.
- (7) Cooper, B. G.; Napoline, J. W.; Thomas, C. M. Catalytic applications of early/late heterobimetallic complexes. *Catal. Rev.: Sci. Eng.* **2012**, *54*, 1–40.
- (8) Neidig, M. L.; Clark, D. L.; Martin, R. L. Covalency in f-element complexes. *Coord. Chem. Rev.* **2013**, *257*, 394–406.
- (9) Kaltsoyannis, N. Does covalency increase or decrease across the actinide series? Implications for minor actinide partitioning. *Inorg. Chem.* **2013**, *52*, 3407–3413.
- (10) Choppin, G. Covalency in f-element bonds. *J. Alloys Compd.* **2002**, *344*, 55–59.
- (11) Cary, S. K.; Vasiliu, M.; Baumbach, R. E.; Stritzinger, J. T.; Green, T. D.; Diefenbach, K.; Cross, J. N.; Knappenberger, K. L.; Liu, G.; Silver, M. A.; DePrince, A. E.; Polinski, M. J.; Van Cleve, S. M.; House, J. H.; Kikugawa, N.; Gallagher, A.; Arico, A. A.; Dixon, D. A.; Albrecht-Schmitt, T. E. Emergence of californium as the second transitional element in the actinide series. *Nat. Commun.* **2015**, *6*, 6827.
- (12) Liu, G.; Cary, S. K.; Albrecht-Schmitt, T. E. Metastable charge-transfer state of californium(III) compounds. *Phys. Chem. Chem. Phys.* **2015**, *17*, 16151–16157.
- (13) Bart, S. C.; Chlopek, K.; Bill, E.; Bouwkamp, M. W.; Lobkovsky, E.; Neese, F.; Wieghardt, K.; Chirik, P. J. Electronic Structure of Bis(Imino)Pyridine Iron Dichloride, Monochloride, and Neutral Ligand Complexes: A Combined Structural, Spectroscopic, and Computational Study. *J. Am. Chem. Soc.* **2006**, *128*, 13901–13912.
- (14) Ivakhnenko, E. P.; Starikov, A. G.; Minkin, V. L.; Lyssenko, K. A.; Antipin, M. Y.; Simakov, V. L.; Korobov, M. S.; Borodkin, G. S.; Knyazev, P. A. Synthesis, molecular and electronic structures of six-coordinate transition metal (Mn, Fe, Co, Ni, Cu, and Zn) complexes with redox-active 9-hydroxyphenoxazin-1-one ligands. *Inorg. Chem.* **2011**, *50*, 7022–7032.
- (15) Ranis, L. G.; Werellapatha, K.; Pietrini, N. J.; Bunker, B. A.; Brown, S. N. Metal and ligand effects on bonding in group 6 complexes of redox-active amidodiphenoxides. *Inorg. Chem.* **2014**, *53*, 10203–10216.
- (16) Pattenau, S. A.; Kuehner, C. S.; Dorfner, W. L.; Schelter, E. J.; Fanwick, P. E.; Bart, S. C. Spectroscopic and structural elucidation of uranium dioxophenoxazine complexes. *Inorg. Chem.* **2015**, *54*, 6520–6527.
- (17) Ivakhnenko, E. P.; Romanenko, G. V.; Simakov, V. I.; Knyazev, P. A.; Bogomyakov, A. S.; Lyssenko, K. A.; Minkin, V. L. Synthesis and structure of nonacoordinated tris-chelate lanthanide (III) complexes with tridentate 2,4,6,8-tetrakis(tert-butyl)-9-hydroxyphenoxazin-1-one ligands. *Inorg. Chim. Acta* **2017**, *458*, 116–121.
- (18) Ivakhnenko, E. P.; Simakov, V. L.; Knyazev, P. A.; Romanenko, G. V.; Bogomyakov, A. S.; Minkin, V. L. Synthesis and structure of a tris-chelate Gd (III) complex with tridentate 2,4,6,8-tetrakis(tert-butyl)-9-hydroxyphenoxazinone ligands. *Mendeleev Commun.* **2016**, *26*, 49–51.
- (19) Pangborn, A. B.; Giardello, M. A.; Grubbs, R. H.; Rosen, R. K.; Timmers, F. J. Safe and convenient procedure for solvent purification. *Organometallics* **1996**, *15*, 1518–1520.
- (20) Apex2 v2014.11; Bruker AXS Inc.; Madison (WI), USA, 2013/2014.
- (21) SHELXTL (version 6.14) (2000–2003) Bruker Advanced X-ray Solutions; Bruker AXS Inc.: Madison, Wisconsin, USA.
- (22) Sheldrick, G. M. *Acta Crystallogr., Sect. A: Found. Crystallogr.* **2008**, *A64*, 112–122.
- (23) Sheldrick, G. M. *Acta Crystallogr.* **2015**, *C71*, 3–8.
- (24) Hübschle, C. B.; Sheldrick, G. M.; Dittrich, B. *J. Appl. Crystallogr.* **2011**, *44*, 1281–1284.
- (25) *CrystalClear*; Rigaku Corp.: The Woodlands, Texas, USA, 2001.
- (26) Otwinowski, Z.; Minor, W. *Methods Enzymol.* **1997**, *276*, 307–327.
- (27) Sheldrick, G. M. *Scalepack*; University of Göttingen: Göttingen, Germany, 2013.
- (28) *Nonius Collect Users Manual*; Nonius Delft: The Netherlands 1998.
- (29) Saint Plus, V8.34A, Bruker Analytical X-ray, Madison, WI, 2009.
- (30) Bain, G. A.; Berry, J. F. *J. Chem. Educ.* **2008**, *85*, 532.
- (31) Olekhovich, L. P.; Simakov, V. L.; Furmanova, N. G.; Ivakhnenko, E. P. Tautomerism and stereodynamics in the series of

sterically hindered ortho-substituted *n*-arylquinonimines. *Dokl. Akad. Nauk* **1999**, 369, 632–638.

(32) Fonseca Guerra, C.; Snijders, G. J.; te Velde, G.; Baerends, E. J. Towards an order-*N* DFT method. *Theor. Chem. Acc.* **1998**, 99, 391–403.

(33) ADF2013, SCM, Theoretical Chemistry; Vrije Universiteit: Amsterdam, The Netherlands, <http://www.scm.com>.

(34) Te Velde, G. T.; Bickelhaupt, F. M.; Baerends, E. J.; Guerra, C. F.; van Gisbergen, S. J. A.; Snijders, J. G.; Ziegler, T. Chemistry with ADF. *J. Comput. Chem.* **2001**, 22, 931–967.

(35) Becke, A. D. Density-functional thermochemistry. III. The role of exact exchange. *J. Chem. Phys.* **1993**, 98, 5648–5652.

(36) Lee, C.; Yang, W.; Parr, R. G. Development of the Colle-Salvetti correlation-energy formula into a functional of the electron density. *Phys. Rev. B: Condens. Matter Mater. Phys.* **1988**, 37, 785–789.

(37) Kim, H.; Choi, J. M.; III Goddard, W. A. Universal correction of density functional theory to include London dispersion (up to *Lr*, element 103). *J. Phys. Chem. Lett.* **2012**, 3, 360–363.

(38) van Lenthe, E.; Baerends, E. J.; Snijders, J. G. Relativistic total energy using regular approximations. *J. Chem. Phys.* **1994**, 101, 9783–9792.

(39) Van Lenthe, E.; Van Leeuwen, R.; Baerends, E. J. Relativistic regular two-component hamiltonians. *Int. J. Quantum Chem.* **1996**, 57, 281–293.

(40) Aquilante, F.; Autschbach, J.; Carlson, R. K.; Chibotaru, L. F.; Delcey, M. G.; De Vico, L.; Galvan, I. F.; Ferre, N.; Frutos, L. M.; Gagliardi, L.; Garavelli, M.; Giussani, A.; Hoyer, C. E.; Manni, L. G.; Lischka, H.; Ma, D.; Malmqvist, P. A.; Muller, T.; Nenov, A.; Olivucci, M.; Pedersen, T. B.; Peng, D.; Plasser, F.; Pritchard, B.; Reiher, M.; Rivalta, I.; Schapiro, I.; Segarra-Martí, J.; Stenrup, M.; Truhlar, D. G.; Ungur, L.; Valentini, A.; Vancoillie, S.; Veryazov, V.; Vysotskiy, V. P.; Weingart, O.; Zapata, F.; Lindh, R. Molcas 8: new capabilities for multiconfigurational quantum chemical calculations across the periodic table. *J. Comput. Chem.* **2016**, 37, 506–541.

(41) Dolg, M.; Stoll, H.; Preuss, H. Energy-adjusted *ab initio* pseudopotentials for the rare earth elements. *J. Chem. Phys.* **1989**, 90, 1730–1734.

(42) Küchle, W.; Dolg, M.; Stoll, H.; Preuss, H. Energy-adjusted pseudopotentials for the actinides. Parameter sets and test calculations for thorium and thorium monoxide. *J. Chem. Phys.* **1994**, 100, 7535–7542.

(43) Cao, X.; Dolg, M. Segmented contraction scheme for small-core lanthanide pseudopotential basis sets. *J. Mol. Struct.: THEOCHEM* **2002**, 581, 139–147.

(44) Cao, X.; Dolg, M. Segmented contraction scheme for small-core actinide pseudopotential basis sets. *J. Mol. Struct.: THEOCHEM* **2004**, 673, 203–209.

(45) Cao, X.; Dolg, M.; Stoll, H. Valence basis sets for relativistic energy-consistent small-core actinide pseudopotentials. *J. Chem. Phys.* **2003**, 118, 487–496.

(46) Aquilante, F.; Malmqvist, P. Å.; Pedersen, T. B.; Ghosh, A.; Roos, B. O. Cholesky decomposition-based multiconfiguration second-order perturbation theory (CD-CASPT2): Application to the spin-state energetics of Co-III(diaminato) (NPh). *J. Chem. Theory Comput.* **2008**, 4, 694–702.

(47) Cotton, S. *Lanthanide and Actinide Chemistry*; John Wiley and Sons: West Sussex, U.K., 2006.

(48) Feng, J.; Zhang, H. Hybrid materials based on lanthanide organic complexes: A review. *Chem. Soc. Rev.* **2013**, 42, 387–410.

(49) Walter, M. D.; Fandos, R.; Andersen, R. A. Synthesis and magnetic properties of cerium macrocyclic complexes with tetramethyldibenzotetraaza[14]annulene, tmtaaH₂. *New J. Chem.* **2006**, 30, 1065–1070.

(50) Behrle, A. C.; Levin, J. R.; Kim, J. E.; Drewett, J. M.; Barnes, C. L.; Schelter, E. J.; Walensky, J. R. Stabilization of M(IV) = Ti, Zr, Hf, Ce, and Th using a selenium bis(phenolate) ligand. *Dalton Trans.* **2015**, 44, 2693–2702.

(51) Stults, S. D.; Andersen, R. A.; Zalkin, A. Chemistry of trivalent cerium and uranium metallocenes: Reactions with alcohols and thiols. *Organometallics* **1990**, 9, 1623–1629.

(52) Evans, W. J.; Hozbor, M. A. Paramagnetism in organo-lanthanide complexes. *J. Organomet. Chem.* **1987**, 326, 299–306.

(53) Tian, G.; Shuh, D. K.; Beavers, C. M.; Teat, S. J. A structural and spectrophotometric study on the complexation of Am(III) with TMOGA in comparison with the extracted complex of DMDOGA. *Dalton Trans.* **2015**, 44, 18469–18474.

(54) Charushnikova, I. A.; Fedoseev, A. M.; Perminov, V. P. Synthesis and structure of complex nitrates of some Ln(III) and of Am(III) with 1,10-phenanthroline-2,9-dicarboxylic acid anions. *Radiochemistry (Moscow, Russ. Fed.)* **2015**, 57, 111–121.

(55) Gagliardi, L.; Lindh, R.; Karlström, G. Local properties of quantum chemical systems: The LoProp approach. *J. Chem. Phys.* **2004**, 121, 4494–4500.

(56) Spivak, M.; Vogiatzis, K. D.; Cramer, C. J.; de Graaf, C.; Gagliardi, L. Quantum chemical characterization of single molecule magnets based on uranium. *J. Phys. Chem. A* **2017**, 121, 1726–1733.

(57) Gaggioli, C. A.; Gagliardi, L. Theoretical investigation of plutonium-based single-molecule magnets. *Inorg. Chem.* **2018**, 57, 8098–8105.

(58) Polinski, M. J.; Garner, E. B., III; Maurice, R.; Planas, N.; Stritzinger, J. T.; Parker, T. G.; Cross, J. N.; Green, T. D.; Alekseev, E. V.; Van Cleve, S. M.; Depmeier, W.; Gagliardi, L.; Shatruk, M.; Knappenberger, K. L.; Liu, G.; Skanthakumar, S.; Soderholm, L.; Dixon, D. A.; Albrecht-Schmitt, T. E. Unusual structure, bonding and properties in a californium borate. *Nat. Chem.* **2014**, 6, 387–392.

(59) Deblonde, G. J. P.; Sturzbecher-Hoehne, M.; Rupert, P. B.; An, D. D.; Illy, M.-C.; Ralston, C. Y.; Brabec, J.; de Jong, W. A.; Strong, R. K.; Abergel, R. J. Chelation and stabilization of berkelium in oxidation state + IV. *Nat. Chem.* **2017**, 9, 843.

(60) Groom, C. R.; Bruno, I. J.; Lightfoot, M. P.; Ward, S. C. The Cambridge Structural Database. *Acta Crystallogr., Sect. B: Struct. Sci., Cryst. Eng. Mater.* **2016**, B72, 171–179.